JOURNAL OF SPACECRAFT AND ROCKETS
Vol. 41, No. 6, November–December 2004

Compressible Wall-Injection Flows in Laminar, Transitional, and Turbulent Regimes: Numerical Prediction

B. Wasistho,* S. Balachandar,† and R. D. Moser†
University of Illinois at Urbana–Champaign, Urbana, Illinois 61801

Numerical simulations of compressible rocket flows are conducted in laminar, transitional, and turbulent regimes. The laminar simulation is carried out on a planar rocket flow without nozzle using the unsteady two-dimensional Navier–Stokes system. The transitional and turbulent flows are performed in three-dimensional on an extended rocket geometry with a divergent outlet using compressible large eddy simulation (LES) models. In both cases, the compressibility effect plays an important role. In the laminar case, pressure oscillation is forced at the outflow boundary. The time-averaged part of the solution is compared with the inviscid theory of compressible rocket flow of Balakrishnan et al. (Balakrishnan, G., Linan, A., and Williams F. A., "Compressibility Effects in Thin Channels with Injection," *AIAA Journal*, Vol. 29, No. 12, 1991, pp. 2149–2154) and the oscillatory part with the acoustic layer model of Majdalani and Van Moorhem (Majdalani, J., and Van Moorhem, W. K., "Improved Time-Dependent Flowfield Solution for Solid Rocket Motors," *AIAA Journal*, Vol. 36, No. 2, 1998, pp. 241–248). The mean flow from the present numerical result is in better agreement with the compressible theory than the conventional Taylor's profiles (Taylor, G. I., "Fluid Flow in Regions Bounded by Porous Surfaces," *Proceedings of the Royal Society of London*, Series A: *Mathematical and Physical Sciences*, Vol. 234, 1956, pp. 456–475), as expected. The oscillatory part of the flow agrees well in the first quarter of the axial extent, near the head end. Farther downstream, the discrepancies develop rapidly between the numerical result and the acoustic-layer model. Possible causes of the difference are the effect of compressibility, which alters the local speed of sound, hence, acoustic properties, and the interference of hydrodynamic instabilities. In the transition and turbulent regimes, the dynamic LES model is applied on different resolutions. The measurements data of Traineau et al. (Traineau, J. C., Hervat, P., and Kuentzmann, P., "Cold Flow Simulation of a Two Dimensional Nozzleless Solid Rocket Motor," AIAA Paper 86-1447, June 1986) are employed for comparison purposes. The refinement study by comparison with the measurement data suggests the importance of resolving the laminar and transition region for a reliable application of LES in transitional flows. With the consideration of this aspect, LES with efficient grid size can produce resonable accuracy. Forcing hydrodynamic instabilities and a more realistic injection fluctuations model are recommended.

I. Introduction

THE core flow inside a solid rocket motor is composed of three different regimes. Near the head end the flow is laminar. Core flow pseudoturbulence and fluctuations originated from the mass injection by the burning solid propellant trigger a transition in the midsection of the chamber and the flow becomes turbulent in the downstream region near the aft end or nozzle. Each regime is characterized by different physical features. The laminar regime is susceptible to many sources of disturbances. In this regime, flow instability constitutes a dominant phenomenon, which strongly influences the structure in the other regimes. In the transition regime, a mixing phenomenon is triggered halfway between the wall and the center of the chamber. This mixing increases in the axial direction, and the peak of the fluctuations amplitude moves toward the wall as desribed by Beddini.[1] In the turbulent regime, the turbulence intensity is concentrated in the vicinity of the wall. This characteristic of turbulent flows intensifies the erosive burning at the propellant surface. In the course of the flow evolving from the laminar through the turbulent regime, the effect of compressibility becomes increasingly important.

Until recently, some simplified models and theoretical relations have been developed to describe the dominant characteristics of each regime separately and to model important physical effects. A theoretical analysis of the two-dimensional inviscid and compressible flowfield has been proposed by Balakrishnan et al.[2] This work provides a more realistic theoretical prediction of rocket flows than the commonly used incompressible theory[3] through the inclusion of compressibility effect. Models for the rotational component of a time-dependent velocity field, termed acoustic layer, were derived by Flandro,[4,5] and an improved solution for the same physical phenomenon has been proposed by Majdalani and Van Moorhem.[6] Both Flandro's and Majdalani and Van Moorhem's models assume a constant amplitude of the irrotational component. In addition to the formulations of the flowfield, the boundary conditions issue, especially that on the entrainment of surface turbulence, has a significant effect on transition prediction. Attempts have been made in this direction, among others by Beddini.[1] However, the results are not satisfactory.

The aforementioned simplified models have often been used in the design and study of solid propellant rocket motors and the stability of rocket combustion. In the present study, we compare some of these models to numerical simulations containing more complete physics to identify the importance of the physics ignored by the models and, in turn, the limitations of the models in certain flow regimes. We use ROCFLO, a code developed in the Center for Simulation of Advanced Rockets, designed to handle the multiphysics phenomena that typically occur inside a rocket flow. For the transition and turbulent cases, a dynamic large eddy simulation (LES) approach is followed. The LES approach in this case is the simplified model for the actual flow, resulting from controlled measurements. In LES, only large scales of fluid motion are resolved. The small scales are modeled using subgrid models. Transitional flow as we study here is a new teritory of LES. Subgrid models are known to be more sensitive to a transitional flow than fully turbulent flow. An LES of transitional flow in a solid rocket motor has been performed by Apte and Yang.[7] They adopt fixed Smagorinsky model with Van

Presented as Paper 2002-4344 at the AIAA/ASME/SAE/ASEE 38th Joint Propulsion Conference, Indianapolis, IN, 7–10 July 2002; received 20 April 2003; revision received 9 December 2003; accepted for publication 23 December 2003.

*Research Scientist, Center for Simulation of Advanced Rockets; wasistho@uiuc.edu. Member AIAA.

†Professor, Department of Theoretical and Applied Mechanics. Senior Member AIAA.

Driest damping in their simulation. This model, however, requires a coefficient to be fixed and is known for its dissipative character. Hence, the model is unsuitable for transitional flows. This can be clearly seen from Apte and Yang's simulation results that underpredict the turbulence level of the measurements by Traineau et al.[8] Their recent work using dynamic LES on the same flow[9] yields improved statistics, even though the resulting turbulence intensity profiles in the core region exhibits constant levels, different from the corresponding measurement. The grid size used in their simulation is large (nearly 9 million cells), which suggests the case to be quasi-direct numerical simulation (DNS), and therefore, a less critical test of the LES model. In the present LES, a dynamic approach is followed. The grid size of our finest resolution is an order of magnitude less than Apte and Yang's, thus, providing a higher challenge for the subgrid models and a better scalability to a full-scale rocket simulation. Because of the lack of a better physical model for mass injection turbulence, random fluctuations with specified amplitude is imposed at the injection boundary.

The paper is organized as follows. In Sec. II, we outline the governing equations, models formulation, and simulation setup. In Sec. III discussions are provided on the results of the laminar cases, whereas in Sec. IV we deal with the transition and turbulent cases. We summarize our findings in Sec. V.

II. Problem Formulation

Compressible flow inside a rocket motor can be described by the time-dependent Navier–Stokes (NS) equations that represent conservation of mass, momentum, and energy:

$$\partial_t \rho + \partial_j(\rho u_j) = S_r \tag{1}$$

$$\partial_t(\rho u_i) + \partial_j(\rho u_i u_j) + \partial_i p - \partial_j \sigma_{ij} = S_{mi} \tag{2}$$

$$\partial_t e + \partial_j((e+p)u_j) - \partial_j(\sigma_{ij}u_i - q_j) = S_e \tag{3}$$

The summation convention is used throughout this paper. The symbols ∂_t and ∂_j denote the partial differential operators $\partial/\partial t$ and $\partial/\partial x_j$, ρ is the density, p is the pressure, u_i is the ith component of the velocity vector, and e the total energy density, given for an ideal gas by

$$e = E(\rho, \boldsymbol{u}, p) = p/(\gamma - 1) + \tfrac{1}{2}\rho u_i u_i \tag{4}$$

where γ is the adiabatic gas constant. Moreover, σ_{ij} is the stress tensor, which is a function of the dynamic viscosity μ and velocity vector $\boldsymbol{u} = [u_1, u_2, u_3]^T$,

$$\sigma_{ij} = \mu(T) S_{ij}(\boldsymbol{u}) \tag{5}$$

where the strain rate tensor S_{ij} is defined as

$$S_{ij} = \partial_j u_i + \partial_i u_j - \tfrac{2}{3}\delta_{ij}\partial_k u_k \tag{6}$$

The dynamic viscosity μ is related to the temperature T by Sutherland's law:

$$\mu(T) = [\beta/(T + C)]T^{\frac{3}{2}} \tag{7}$$

where $C = 110.4$ K and $\beta = 1.456 \times 10^{-6}$ kg/ms. Finally, q_j is the jth component of the heat flux vector, defined as

$$q_j = Q_j(T) = -(\mu C_p/Pr)\partial_j T \tag{8}$$

where C_p is the specific heat at constant pressure. The temperature is related to the density and the pressure by the ideal gas law. The right hand side S_r, S_{mi}, and S_e are source terms for the mass, momentum, and energy conservation equations, respectively, which are nonzero only for a validation test case called compressible periodic rocket (CPR). The expressions for these source terms are given in Sec. II.C. Throughout, we use $\gamma = 1.4$ and molecular Prandtl number $Pr = 0.72$.

The system of equations is solved directly for flow simulations in the laminar regime. The equations are discretized in time using an explicit four-step Runge–Kutta method. A second-order finite volume central scheme is used for spatial discretization. Specifically, the scheme is based on cell-centred control volumes for the convective term. The code provides provision for added second- and fourth-order artificial dissipation for enhanced stability. These artificial dissipations are, however, not used in the present simulations when computing turbulence cases using LES. The convective fluxes through a face of the control volume are approximated using the average of variables. A detailed description of this scheme may be found in Ref. 10. The viscous terms are discretized in the same way, making use of an auxiliary control volume shifted by a half grid cell in each computational direction. The auxiliary control volumes are for the first derivatives and the primary ones (grid cells) for the second dervatives of the viscous terms.

For flows involving turbulence, we use the LES approach. In LES the NS equations are spatially filtered. The filtered solution $\bar{f}$ is related to f as

$$\bar{f}(\boldsymbol{x}, t) = \int_\Omega G(\boldsymbol{x} - \boldsymbol{\xi}) f(\boldsymbol{\xi}, t)\, \mathrm{d}\boldsymbol{\xi} \tag{9}$$

where $\boldsymbol{x}$ and $\boldsymbol{\xi}$ are coordinate vectors in the flow domain Ω. For the filter function G, we use the top hat filter.[11] Applying the filtering operation to the NS equations, assuming zero source terms for convenience, we obtain

$$\partial_t \bar{\rho} + \partial_j(\bar{\rho}\tilde{u}_j) = 0 \tag{10}$$

$$\partial_t(\bar{\rho}\tilde{u}_i) + \partial_j(\bar{\rho}\tilde{u}_i\tilde{u}_j) + \partial_i \bar{p} - \partial_j \breve{\sigma}_{ij} = F_i \tag{11}$$

$$\partial_t \breve{e} + \partial_j((\breve{e} + \bar{p})\tilde{u}_j) - \partial_j(\breve{\sigma}_{ij}\tilde{u}_i - \breve{q}_j) = F_e \tag{12}$$

where the additional momentum and energy subgrid terms appearing on the right-hand side are given by

$$F_i = -\partial_j(\bar{\rho}\tau_{ij}) + \partial_j(\bar{\sigma}_{ij} - \breve{\sigma}_{ij}) \tag{13}$$

$$F_e = \alpha_1 + \alpha_2 + \alpha_3 + \alpha_4 \tag{14}$$

The filter operation given by Eq. (9) is denoted by an overbar, and a tilde indicates Favre filtering[12] and $\bar{\sigma}_{ij}$ and $\bar{q}_j$ denote the stress tensor and heat flux vector, respectively, expressed in filtered field variables. The energy subgrid term is composed of several components,[13] which are α_1, representing the kinetic energy transfer from resolved to subgrid scales; α_2, the effect of subgrid turbulence on the resolved heat conduction; α_3, the pressure dilatation; and α_4, the subgrid turbulence dissipation rate. Expressions for these terms may be found in Ref. 13.

A. Subgrid Stress Models

In this study, the dynamic eddy viscosity model for the turbulent stress tensor $m_{ij} = \bar{\rho}\tau_{ij}$ is employed:

$$m_{ij} = -\mu_t S_{ij}(\tilde{\boldsymbol{u}}) \tag{15}$$

$$\mu_t = \bar{\rho} C_d \Delta^2 |S(\tilde{\mathbf{u}})| \tag{16}$$

where S_{ij} is the strain rate tensor defined by Eq. (6). The coefficient C_d is determined dynamically using the Germano et al. identity[14]

$$\hat{\bar{\rho}} T_{ij} - \widehat{\bar{\rho}\tau_{ij}} = L_{ij} \tag{17}$$

where the overbar filter denotes the basic filter corresponding to the filter width Δ, whereas the hat filter denotes the test filter corresponding to a filter width 2Δ. In the preceding identity, the subgrid stress on the test filter level $\hat{\bar{\rho}} T_{ij}$ is given by

$$\hat{\bar{\rho}} T_{ij} = \widehat{\overline{\rho u_i u_j}} - \widehat{\bar{\rho}\bar{u}_i}\,\widehat{\bar{\rho}\bar{u}_j}/\hat{\bar{\rho}} \tag{18}$$

This yields

$$C_d = \text{maximum}\left(0, \frac{\langle M_{ij} L_{ij}\rangle}{\langle M_{ij} M_{ij}\rangle}\right) \tag{19}$$

where

$$L_{ij} = (\overline{\rho u_i}\,\overline{\rho u_j}/\bar{\rho})\hat{} - \widehat{\overline{\rho u_i}}\,\widehat{\overline{\rho u_j}}/\hat{\rho} \tag{20}$$

$$M_{ij} = -\hat{\bar{\rho}}(2\Delta)^2|S(\boldsymbol{v})|S_{ij}(\boldsymbol{v}) + \left[\bar{\rho}\Delta^2|S(\tilde{\boldsymbol{u}})|S_{ij}(\tilde{\boldsymbol{u}})\right]\hat{} \tag{21}$$

where the symbol $\langle\cdot\rangle$ is an averaging operator over the homogeneous direction (in the present study, the spanwise direction) and $\boldsymbol{v}$ is the Favre-filtered velocity vector on the test filter level. The notation $(\,)\hat{}$ denotes that the hat filter is applied to the term between the brackets.

B. Subgrid Energy Models

In the modeling of the energy subgrid terms, the kinetic-energy transfer term α_1 can be computed directly from the model of the turbulent stress tensor m_{ij} in the momentum equation. This term is expressed as

$$\alpha_1 = \widetilde{u_i}\,\partial_j(\bar{\rho}\tau_{ij}) \tag{22}$$

The sum of the heat conduction and pressure dilatation terms is lumped together using the turbulent heat conductivity model,[15] similar to Eq (8):

$$\alpha_2 + \alpha_3 = -(\mu_t C_p/Pr_t)\partial_j T \tag{23}$$

where μ_t is the modeled eddy viscosity and Pr_t the turbulent Prandtl number, set to 0.9 rather than determined dynamically. The dissipation-rate term α_4 is modeled using the k-equation model[16]:

$$\alpha_4 = c_\epsilon \bar{\rho}\left(k^{\frac{3}{2}}/\Delta\right) \tag{24}$$

with $k = \frac{1}{2}\tau_{ii}$, and c_ϵ is determined dynamically assuming a global balance between the kinetic energy transfer and the dissipation rate.

C. Validation

The validation of the LES model and the code is first performed in the context of a CPR. The computational configuration is formed by a planar periodic channel with mass injection at the top and bottom walls, as shown in Fig. 1. The dimension of the domain is $2\pi h \times h \times \pi h$, where $h = 0.01$ m is the same as the height of the rocket chamber to be considered later. For the CPR simulation, the computational geometry captures only small streamwize segment of the rocket located at a chosen streamwize location. The governing fluid equations are modified to enforce streamwise periodicity. Source terms S_r, S_{mi}, and S_e that appear in the conservation equations (1–3) result from this homogenization procedure.[17] These source terms read

$$S_r = -\epsilon\langle\rho u_1\rangle \tag{25}$$

$$S_{mi} = -\epsilon\left\langle\rho u_1 u_i + \delta_{i1}\left(\rho u_1^2 + \delta_s p\right)\right\rangle \tag{26}$$

$$S_e = -\epsilon\langle(e+p)u_j\rangle \tag{27}$$

where $\langle\cdot\rangle$ denotes averaging over the homogeneous directions (stream and spanwise) and $\epsilon = m_{\text{inj}}/m_b$ is the ratio between injection and bulk mass rate. The quantity $\delta_s p = \delta p/\delta x_s$, where $x_s = \epsilon x$, is a pressure gradient to be determined from the mass flux balance. Physically, S_r compensates the mass added through the injection walls, whereas S_{mi} and S_e balance the acceleration and the corresponding increase of energy due to the increase in mass flux in the streamwise direction.

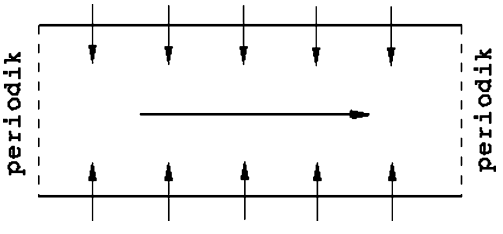

Fig. 1 Schematic of CPR simulation domain for LES validation.

We perform two LES cases of CPR at injection Reynolds number 190 and 7840 with use of grid resolution $95 \times 95 \times 47$ and $95 \times 65 \times 33$, respectively. These LES results are compared against the DNS results of Venugopal[17] performed at injection Reynolds number 190. The filter width to grid spacing ratio used in the LES is two for the basic filter. We show comparisons in mean streamwise and wall normal momentum, mean density, and mean temperature, normalized by the injection and head end values in Fig. 2. The mean flow of LES resulting from both Reynolds numbers compares satisfactorily with the DNS data. Unlike in turbulent channel flow, the effect of Reynolds number is insignificant in the mean flow. This is expected because in injection-driven flow in which the boundary layer is blown off from the wall, the effect of wall damping to small-scale turbulent vortices vanishes, hence, the effect of Reynolds number. The fact that different grid resolutions produce virtually the same result demonstrates the grid independency of the present simulations. The result in turbulence statistics is presented by the comparison in rms of density fluctuations in Fig. 3. A good agreement is achieved between LES and DNS. Although the mean flow is virtually unchanged with Reynolds number, the turbulence quantity is clearly affected, in that the peak of the rms quantity shifts toward the injection wall. The effect is similar to that observed in turbulent channel flow, albeit smaller. The overall result is encouraging to apply LES in a spatially evolving flow driven by injection.

D. Geometry

We define two simulation domains for the laminar and turbulent cases. The simulation domain for the laminar case is shown in Fig. 4 by the solid line. It represents a two-dimensional planar channel with uniform flow injection at the top and bottom wall and a no-slip wall at the head end. The domain is truncated at the axial distance of 45 cm from the head end. Hence, the outflow boundary is located upstream of the point where choking would occur. The half channel height is $h = 1$ cm, which is used in the normalization of length scales. The flow is perturbed by oscillating the pressure at the outlet. For the transition and turbulent cases, the geometry is extended to three-dimensions in the spanwise direction by 4 cm as well as in the axial direction (dashed line in Fig. 4) to mimic the same geometry of the measurements by Traineau et al.[8] A periodic boundary condition is applied to the spanwise direction, and random fluctuations of prescribed rms value are added to the mean injection at the top and bottom walls. The grid size is 110×131 for the laminar case. For the turbulent case, two sets of grid are employed with different resolutions and wall normal stretchings, namely, $210 \times 64 \times 32$ and $420 \times 64 \times 32$, in the axial, normal, and spanwise directions, respectively. Although the wall normal grid points are the same, the finer grid has a greater wall normal stretching ratio, which results in smaller normal grid spacings near the wall than the coarser one. As mentioned earlier, the laminar case is performed by DNS and the turbulent case by LES. In the direction normal to the wall, the laminar case employs more grid points to capture the unsteady acoustic layer accurately.

III. Laminar Regime

In this laminar test case, the following parameters are prescribed: injection velocity $v_{\text{inj}} = 3.1$ m/s, injection Reynolds number $Re_{\text{inj}} = 1.85 \times 10^3$, wall temperature $T_w = 260$ K, and mean outlet pressure $p_{\text{out}} = 180{,}000$ N/m^2. A sinusoidal pressure oscillation is excited at the outflow boundary with an amplitude of 1% of the mean value. The resulting oscillation at $x/h = 32$ can be seen in Fig. 5, from which the nondimensional angular frequency can be measured to be $\omega = 29.25$. The result reported in this paper is an improvement of that presented by Wasistho et al.[18] through a fine tuning of the prescribed outlet pressure.

A. Mean Flow

We average the solution in time and compare the resulting mean flow to the corresponding theoretical results of Balakrishnan et al.[2]

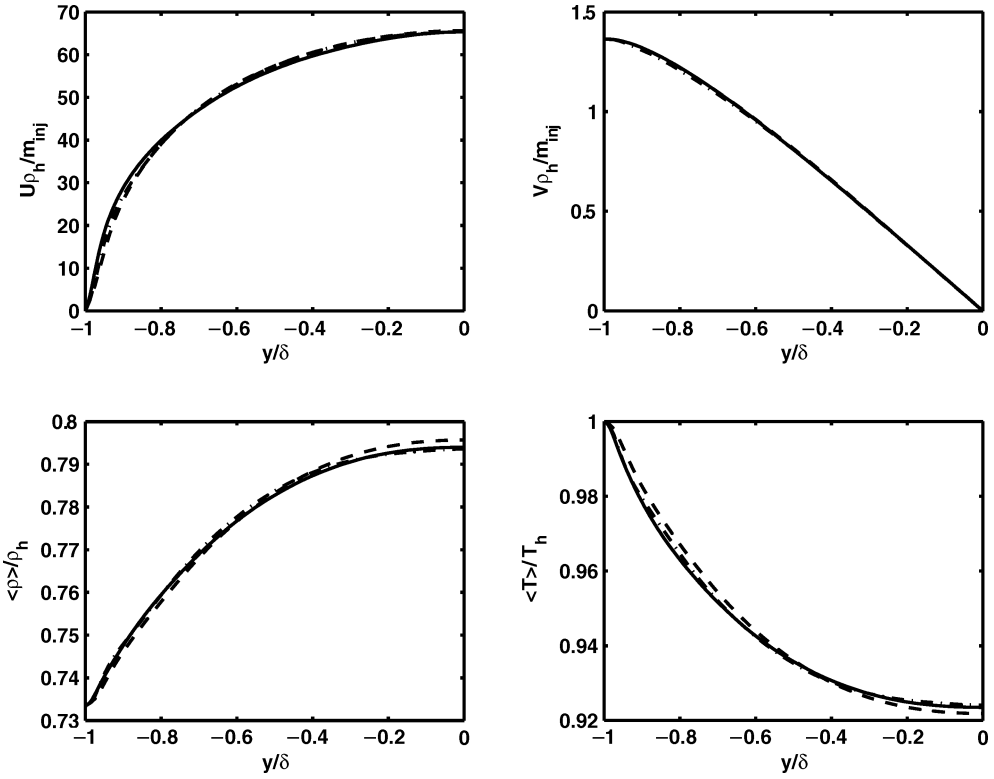

Fig. 2 Mean flow comparison in streamwise momentum, wall normal momentum, density, and temperature, respectively, between ——, DNS at $Re_{inj} = 190$; – – –, LES at $Re_{inj} = 190$; and –·–, LES at $Re_{inj} = 7840$.

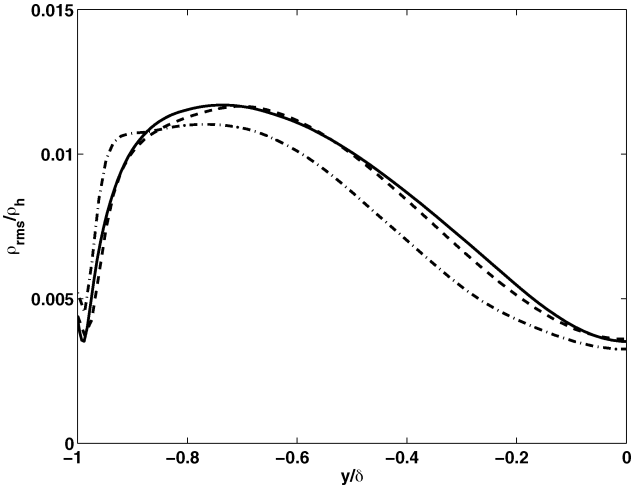

Fig. 3 LES and DNS of r.m.s of density fluctuations non dimensionalized by head end density: ——, DNS at $Re_{inj} = 190$; – – –, LES at $Re_{inj} = 190$; and –·–, LES at $Re_{inj} = 7840$.

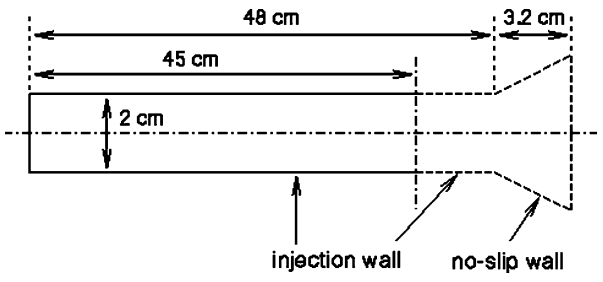

Fig. 4 Schematic of flow domain: ——, laminar, direct simulations and – – –, (extended), turbulent, LES simulations.

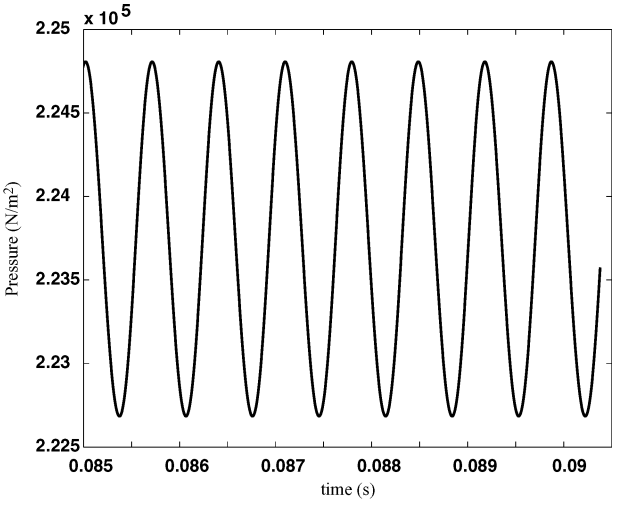

Fig. 5 Pressure oscillation at $x/h = 32$ as function of time.

The results are built on the assumption of inviscid compressible flow in thin injection channels with no tranverse pressure variation, $\partial_2 p = 0$. The problem is parabolic in that, by solving an integral equation for pressure, the velocity and temperature profiles can be determined through algebraic relations. No downstream boundary condition is needed. The resulting pressure and centerline axial velocity distribution from the theory are shown in Figs. 6 and 7 (dashed lines), respectively, compared to the present numerical results (solid lines). The numerical simulation results are in good agreement with the theory in both pressure and axial velocity. This indicates the compressibility effect is captured correctly as the axial velocity increases along the streamwise direction compared to its incompressible counterpart due to the decrease in density.

A comparison of the cross-sectional profiles is shown in Fig. 8 for the axial velocity and in Fig. 9 for the temperature for several axial stations. The agreement with the theory is again favorable in

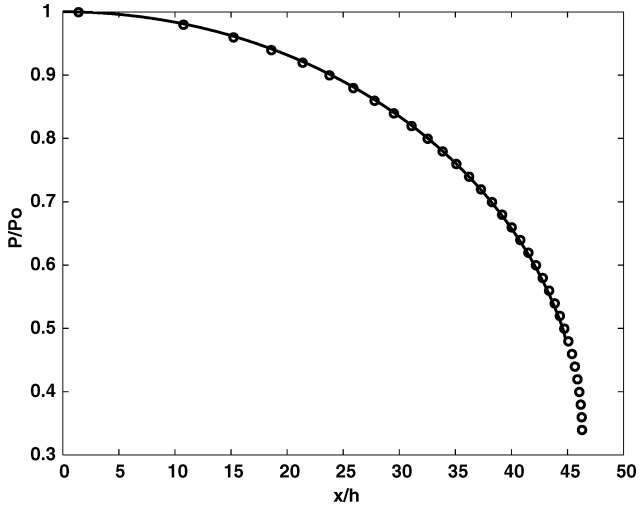

Fig. 6 Static pressure distribution in axial direction: ○, compressible integral formulations and ——, present laminar simulation.

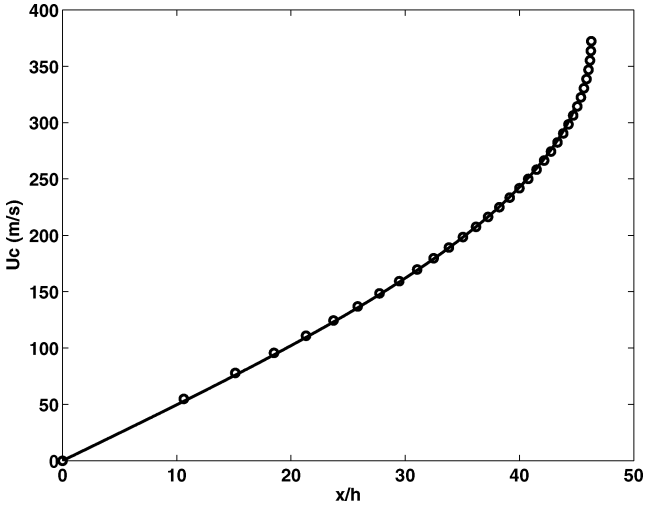

Fig. 7 Axial velocity distribution at centerline: ○, Compressible integral formulations and ——, present laminar simulation.

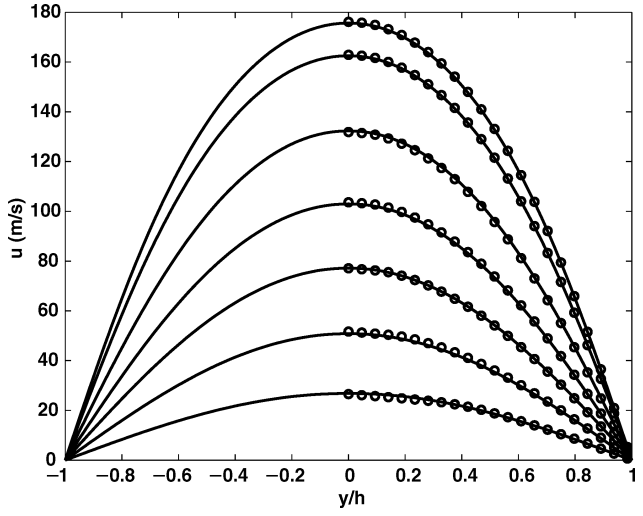

Fig. 8 Streamwise velocity profiles at locations $x/h =$ 5, 10, 15, 20, 25, 30 and 32, obtained from ○, compressible integral formulations and ——, present numerical simulation.

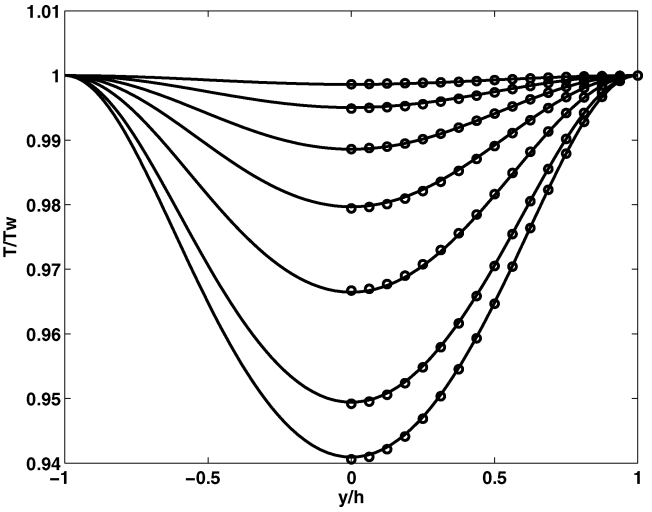

Fig. 9 Similar to Fig. 8 for temperature profiles.

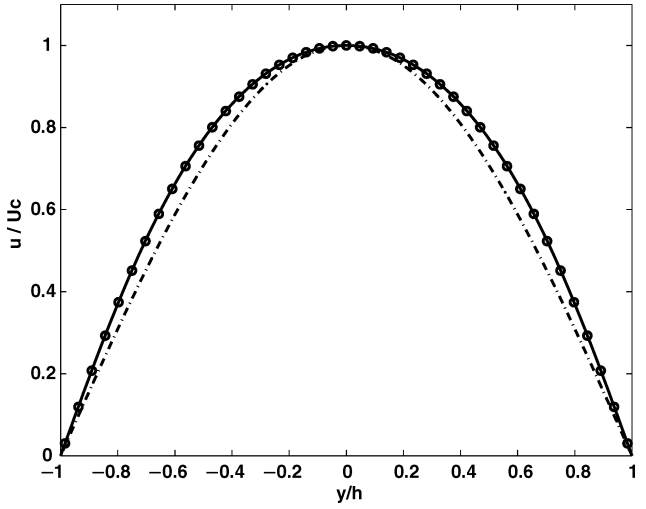

Fig. 10 Normalized streamwise velocity profiles at locations $x/h = 32$, obtained from ○, compressible integral formulations; ——, present numerical simulation; and –·–, Taylor's profile.

both the temperature and velocity profiles. The comparison is done in dimensional form, without any normalization. From the axial decrease of pressure and temperature, it can be derived that the density also decrases in virtually the same magnitude as the pressure in the axial direction. To show the effect of compressibility on the shape of the velocity profile, we include the incompressible profile in Fig. 10 and normalize the data by their centerline values. The data are taken from the axial location $x/h = 32$. The profile from the simulation (solid line) is indiscernible from that of the compressible theory (dashed line), but both are different from Taylor's profile[3] (dashed–dotted line) in that the compressible profile is more convex than the incompressible solution. The flow at this location reaches a Mach number of 0.5, which indicates that compressibility, even at moderate levels, alters the mean flow profiles. Farther downstream, up to the sonic condition at the throat (choking location), the difference is more significant.

We have conducted both viscous and inviscid simulations for the laminar case and observe that the effect of viscosity is negligible. Also observe that the pressure variation in the normal direction is negligible compared to that in the axial direction, thus, validating the assumption employed in the compressible mean flow theory of Balakrishnan et al.[2]

B. Acoustic Layer

The unsteady component of the flow is extracted by substracting the mean solution from the total solution. The analysis of the

unsteady component of the flow employes the acoustic layer model by Majdalani and Van Moorhem[6] as a reference. This model assumes that the flow can be separated into a base flow component $M_b U(x_2)$ with M_b the injection Mach number and $U(x_2)$ given by Taylor's profile and a time-dependent component $u(x_1, x_2, t)$, which in turn is composed of rotational and nonrotational components,

$$u(x_1, x_2, t) = \hat{u}(x_1, t) + \bar{u}(x_1, x_2, t) \tag{28}$$

The nonrotational (or acoustic) component is given by

$$\hat{u}(x_1, t) = iA_p/(p_0\gamma)\sin(\bar{x}_1)e^{-i\bar{t}} \tag{29}$$

and the rotational component $\bar{u}(x_1, x_2, t)$ is defined such that the superposition of the two results in

$$u(x_1, x_2, t) = A_p/(p_o\gamma)[\sin\bar{x}_1 \sin\bar{t} - \sin\theta \sin(\bar{x}_1 \sin\theta)e^{\zeta} \sin(\bar{t} + \Phi)] \tag{30}$$

In the preceding expressions, $\bar{x}_1 = k_m x_1$ and $\bar{t} = k_m t$, with k_m the wave number, and θ is a parabolic function of the distance normal to the wall that vanishes at the centerline. Here $\zeta = \zeta(x_2)$ is a damping function and $\Phi = \Phi(x_2)$ is a phase angle, both of which vary in the wall normal direction. A_p/p_o is pressure wave amplitude relative to the mean chamber pressure. Note that the rotational part of the time-dependent component is attenuated in the core region and vanishes at the center of the channel due to the function θ vanishing there.

The periodic excitation of the outlet presure results in nonrotational waves along the centerline. Comparing with the acoustic layer model represented by Eq. (29), we found that the numerical results best compare with the acoustic model at wave mode $m = 4.5$, which implies that the chamber contains 2.25 waves. This corresponds to wave number $k_m = 0.3156$, kinetic Reynolds number $Re_k = k_m Re_a = 0.62 \times 10^5$, and Strouhal number $Sr = 33.18$, where Re_a is Reynolds number based on the sound speed. Even at this matching wave number, the irrotational or freestream velocity wave only agrees within the first quarter of the axial extent, as can be seen clearly in Fig. 11. In Fig. 11 the simulation result (solid line) is taken from centerline data. The results are compared at the opposite phase to show the difference more clearly. Specifically, the simulation indicates that the wave frequency and amplitude increase in the axial direction. Within the first quarter of the axial extent, where the acoustic component closely follows the model prediction, we are able to compare the wall normal profile of the unsteady velocity, as can be seen in Fig. 12. The pattern from the model prediction closely follows the simulation result up to $x/h = 8$, after which the agreement deteriorates due to the divergence in the acoustic component.

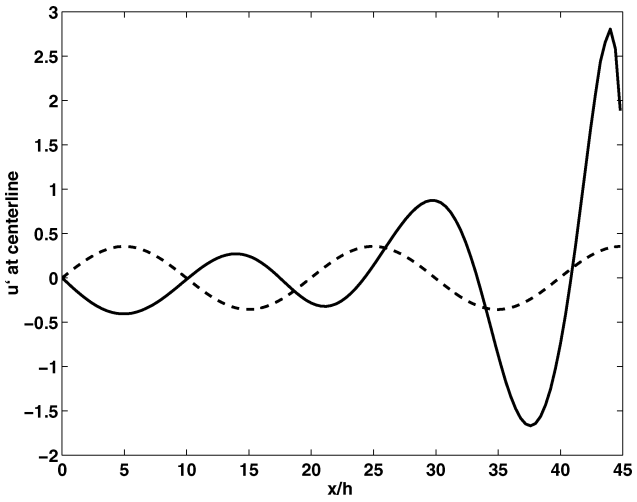

Fig. 11 Unsteady axial velocity fluctuations at centerline: ——, present laminar simulation compared to – – –, model of Majdalani and Van Moorhem[6]; results are compared at opposite phase to show the difference more clearly.

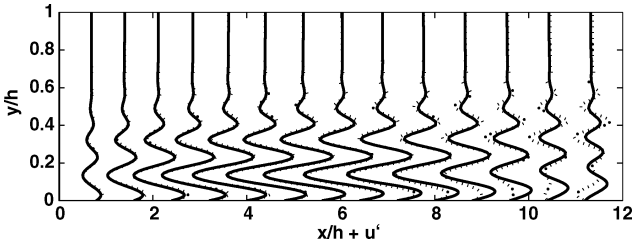

Fig. 12 Snapshot of unsteady axial velocity fluctuations in wall normal direction at first quarter of axial extent: ——, present laminar simulation compared to . . . . , model of Majdalani and Van Moorhem.[6]

We suspect that the discrepancy in the acoustic component is due to the increasing compressibility effect in the axial direction, which is not taken into account in the simplified model. With the increase of Mach number, the temperature in the core flow decreases, rendering a decrease in the local speed of sound, hence, altering the acoustic property of the medium. How this correlates with the increase of amplitude and frequency, however, needs further clarification. Another possibility is that the excited wave has developed to its natural (hydrodynamic) instability in the flow. The instability analysis of Taylor mean profiles by Casalis et al.[19] suggests that the present simulation at the injection Reynolds number $Re_{\text{inj}} = 1.85 \times 10^3$ and nondimensional angular frequency $\omega = 29.25$ (which can be derived from the pressure oscillation in Fig. 5) is in the unstable regime. One can also argue that the difference in the base flow assumption may contribute to the discrepancy. (Taylor's profile[3] is used in the model, whereas the mean flow of the simulation matches with the Balakrishnan et al.[2] profile.) However, as shown by Casalis's stability analysis,[19] Taylor's profile also results in an unstable mode using the earlier values of the angular frequency and injection Renolds number. This reasoning suggests that the acoustic mode with constant amplitude may only be excited at a very low frequency $\omega < 20$ to travel along the neutral curve. Further investigations are required along both of these lines. At this point, it is sufficient to suggest that incorporation of the axial evolution of the mean flow property may increase the fidelity of the acoustic-layer model.

IV. Transition to Turbulent Regime

The study of the laminar regime of the rocket flow in Sec. III is extended to transition and turbulent regimes using the dynamic LES approach outlined in Sec. II. No coefficient needs to be tuned. Instead, all model parameters evolve dynamically according to the state of the flow. We also avoid the use of any artificial dissipation because it may interfere with physical dissipation. As described earlier, the flow domain for the turbulent case is the whole extent of the geometry shown in Fig. 4 with the spanwise extent of 4 cm, which mimics the experimental apparatus of Traineau's cold-flow measurements.[8] The same physical parameters and boundary conditions are also employed in the present study. To imitate the injection through the porous wall, a mass injection boundary condition is invoked and a random fluctuation with specified amplitude is imposed on the mean to trigger and sustain the three dimensionality of the flow.

We perform a grid-refinement study by considering two LES cases as shown in Table 1. Both cases employ the dynamic Smagorinsky subgrid stress model and full energy subgrid models described in Sec. II. The amplitude of the injection mass rate fluctuations at the walls is 5% of the mean value. In Table 1, c and f denote the coarse and fine grids used in each case. The filter width ratio, defined as the ratio of the basic filter width to the local grid spacing, is one for DSE05c and two for DSE05f. The reason for the difference is merely to compensate for the difference in the spacing due to different resolutions. A lower ratio tries to resolve smaller eddies, that is, of the grid-cell size in the coarse grid case, which is assumed comparable to two grid-cells size in the finer grid. Therefore, the filter width ratio two is used in DSE05f. In general, the choice of filter width ratio does not strongly influence the results because the model coefficient adjusts accordingly, as will be seen.

Table 1 Two dynamic LES cases[a] of transitional flow

Case	$N_x \times N_y \times Nz$	Δ/dx_i
DSE05c	$210 \times 64 \times 32$	1
DSE05f	$420 \times 64 \times 32$	2

[a]Injection fluctuation level in both cases is 5% of the mean injection mass rate.

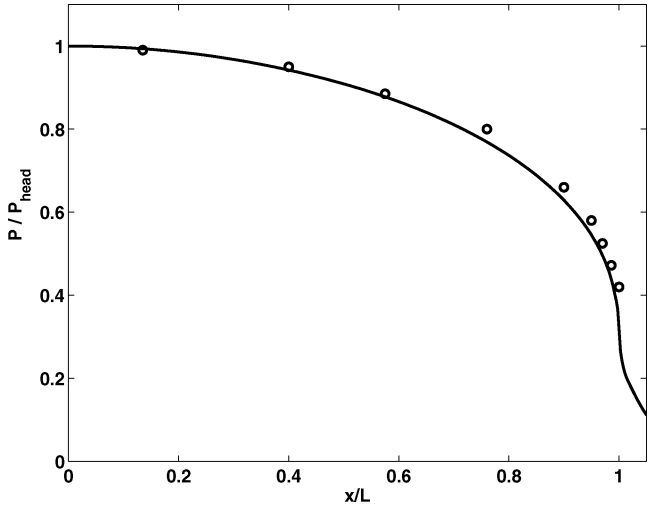

Fig. 13 Static pressure distribution in axial direction: ——, present simulation compared to ○, Traineau et al.[8] experiment.

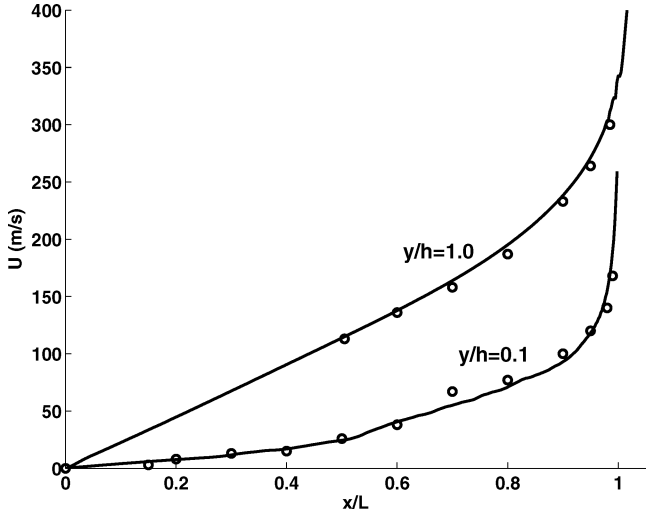

Fig. 14 Same comparison as Fig. 13 for mean axial velocity distribution in axial direction at $y/h = 1.0$ (centerline) and 0.1 (near wall).

A. Mean Flow

We extract the mean quantities by time averaging of the solution after the simulation reaches a statistically stationary condition. The averaging interval is four times flow through, sufficiently long to ensure the invariancy of the averaged quantities with the size of the interval. The agreement of the mean flow between both LES cases and the measurement data is satisfactory. This is represented for case DSE05f by the comparison of the static pressure distribution in Fig. 13 and axial velocity at the centerline and near the wall in Fig. 14. The coarser grid case DSE05c generates virtually the same results. The axial pressure distribution is relatively easy to predict because its derivation from the momentum balance is strightforward due to its invariance in the cross-sectional directions. In comparison, accurate prediction of axial velocity distribution is more difficult because it depends on the velocity profiles in the wall normal direction, which rely on the LES model used. Thus, the agreement

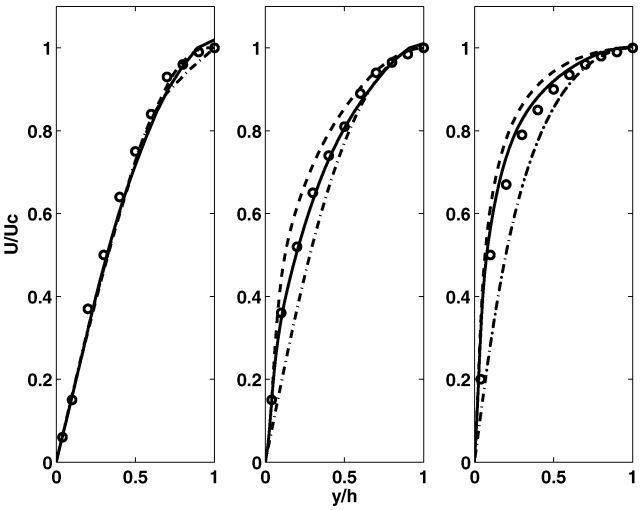

Fig. 15 Streamwise velocity profiles normal to injection wall at axial locations $x/h = 3.45$, 33.01, and 47.00: ○, measurement data by Traineau et al.[8] compared to ——, LES cases DSE05f and – – –, DSE05c; and –·–, Balakrishnan et al.[2] compressible laminar profiles.

seen in Fig. 14 provides confidence in the LES approach. A comparison of Figs. 7 and 14 shows that the centerline axial velocity of the transitional flow is lower than that of the laminar flow. This is expected because, for the same bulk mass flux, a turbulent (fuller) profile implies a lower centerline value than a laminar (shallower) profile.

The evolution of the axial velocity profiles from the laminar to the turbulent state is depicted in Fig. 15. Moreover, this figure shows a comparison of the two LES cases against Traineau's experiment.[8] The compressible theoretical solution of Balakrishnan et al.[2] is included to indicate the effect of turbulence. At $x/h = 3.45$, the LES cases and the measurement data collapse to the compressible laminar profile, which should be virtually the same as Taylor's profile because the compressibility effect is very small near the head end. At a transition and turbulent locations, $x/h = 33.0$ and $x/h = 47.0$, respectively, the effect of turbulence is clearly seen from the more convex profile of the experiment compared to the laminar theory. The coarse grid LES overpredicts the velocity profiles from the experiment at these locations, whereas the finer grid LES produces very good agreement with the experiment.

B. Transition

An important advantage of the dynamic LES approach compared to other turbulence prediction methods is its inherent feature of transition prediction. A common way of detecting transition in an injection driven flow is to examine the distribution of the momentum flux coefficient β defined by

$$\beta = \frac{1}{\bar{u}_b^2 h} \int_o^h \bar{u}^2 \, \mathrm{d}x_2 \tag{31}$$

where $\bar{u}$ is the mean axial velocity and $\bar{u}_b$ the bulk velocity. A comparison of this quantity between the two LES cases (lines) and the experiment (symbols) is provided in Fig. 16. In a fully laminar flow, the momentum flux coefficient is a constant for incompressible case with $\beta \approx 1.235$. In the corresponding compressible case, this function decreases monotonically in the axial direction due to the change of the velocity profile as shown by the laminar theory in Fig. 15. The monotonicity is disturbed by a steep drop if transition occurs, as seen in Fig. 16. The lower value of β in the laminar regime of the experiment,[8] is due to pseudoturbulence. The transition in the experiment starts at $x/h = 20$. The coarse grid LES predicts transition to begin at about $x/h = 11$, whereas the finer grid case predicts a location closer to the experiment, about $x/h = 18$.

When the momentum flux coefficient is used, the extent of a transition process can in fact be detected only vaguely because the

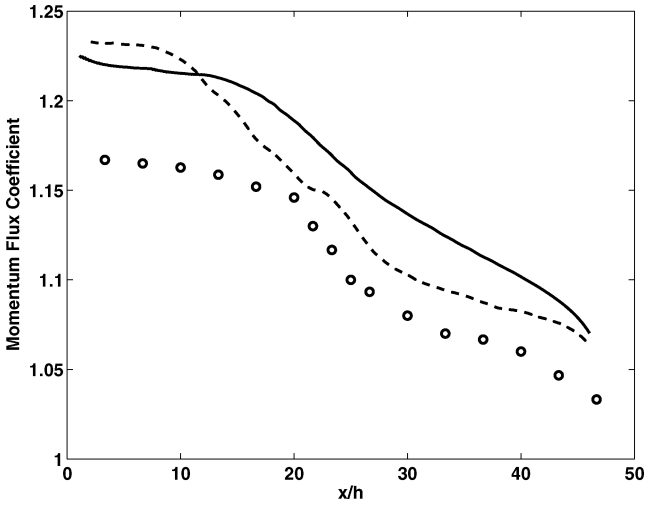

Fig. 16 Axial distribution of momentum flux coefficient: ○, measurement data by Traineau et al.[8] compared to LES cases ——, DSE05f and – – –, DSE05c.

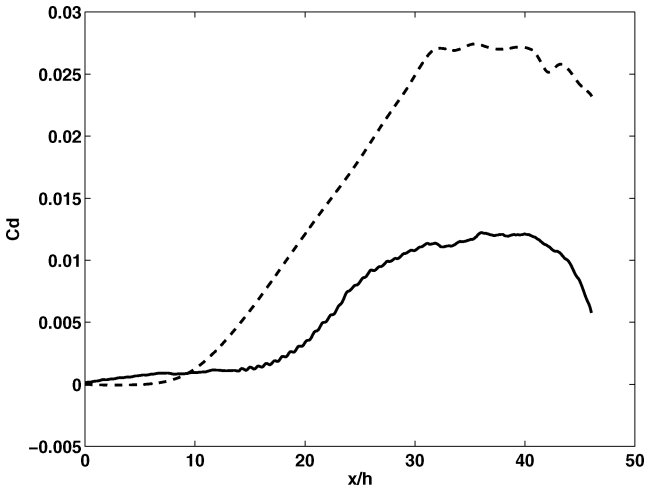

Fig. 17 Axial distribution of model coefficient C_d in dynamic Smagorinsky model: ——, DSE05f and – – –, DSE05c.

function is inherently decreasing in the absence of transition. This is clearly the case with the finer grid LES, where the function keeps decreasing smoothly up to the aft region before entering the nozzle. An alternative way of detecting transition in the dynamic LES is by examining the dynamic coefficient C_d, represented by Eq. (19). The axial distribution of this coefficient, averaged in time and over transversal directions, is shown in Fig. 17. Besides the starting of transition, the dynamic coefficient also shows more clearly where the flow becomes turbulent, in the sense of C_d being saturated. Based on this quantity, the turbulent region starts at approximately $x/h = 31$. The saturation level of C_d is about 0.027 for the coarse grid LES and 0.012 for the finer case. The difference in the level of C_d between the two cases is due to the difference in the basic filter width ratio. The ratio is one for the coarse grid LES and two for the finer grid case as already noted. As can be seen from the expression of the eddy viscosity model in Eq. (16), a higher delta results in a lower C_d to maintain the level of eddy viscosity that is determined by the physics of the flow. It will be shown that the grid independency of LES result, which is the primary feature of LES, can virtually be achieved in the region where C_d levels off.

C. Turbulence Quantities

To assess the turbulence prediction of the LES approach, we perform comparisons of second moment variables, such as turbulence intensity and shear stresses. As mentioned earlier, the axial fine

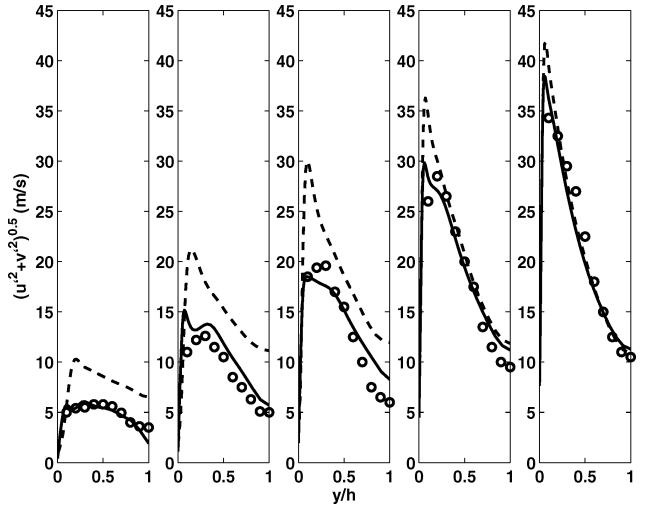

Fig. 18 Turbulence intensity profiles normal to injection wall at axial locations $x/h = 14.99$, 24.00, 30.13, 40.46, and 45.97: ○, measurement data by Traineau et al.[8] compared to LES cases –·–, DSE05f and – – –, DSE05c.

grid resolution is twice the coarse grid. The grid in the wall normal direction is stretched in both cases with more grid points concentrated near the injection wall for the fine grid case. No artificial dissipation is employed to avoid uncertainty coming from its interference with the physical dissipation. Spurious numerical residuals are controlled merely through grid manipulation (refinement and stretching). The physical source of turbulence comes from the wall injection fluctuations and the nonlinear interactions of hydrodynamic instabilities.

The result for the turbulence intensity is shown in Fig. 18 at five axial locations to demonstrate the evolution of the transition process. In Fig. 18, the earlier onset of transition in the coarse grid LES, as seen in the axial development of C_d, is confirmed. This earlier transition is apparently due to large disturbances that occur in the laminar region as a combination of injection fluctuations and numerical residuals. As a result, the turbulence intensity at the center, as well as near the wall, is overpredicted throughout the transition process before the saturation begins. The measured intensity level at $x/h = 24.0$ has been reached at $x/h = 14.99$ in the coarse grid LES. In addition, the peak of the intensity profiles is sharper than observed in the experiment. The finer grid LES on the other hand maintains the disturbances in the laminar region at about the same level as the pseudoturbulence in the experiment. The intensity level and the peak profile of the fine grid case are also in much closer agreement with the experiment. The difference between the coarse and fine case becomes smaller with increasing turbulence. Although not shown here, examination of the overall stress distribution leads to the same assessment as for the turbulence intensity.

This result, in conjunction with the axial development of C_d already discussed, suggests that grid independence of LES can be achieved in the saturated region of the model coefficient. In the developing region of C_d, adequate grid is required through consecutive refinement and clustering. Return to the discussion on the mean velocity profiles shown in Fig. 15: At this point, it is clear that the overprediction of the coarse grid profiles in the transition and turbulent regions is due to the unresolved laminar region.

To investigate whether the flow has reached a fully turbulent state in that the energy cascade has reached down to the grid size, we examine the velocity spectra of the coarse grid case by way of illustration. The fine grid case gives a similar picture. The spectra are computed from the temporal fluctuations of the axial velocity and are plotted in Fig. 19 for four axial locations, all in the saturated region of C_d. The spectra do not contain an inertial range displaying the $-\frac{5}{3}$ law. Because of the relatively coarse mesh used in these simulations, the small scales are most likely dissipated by

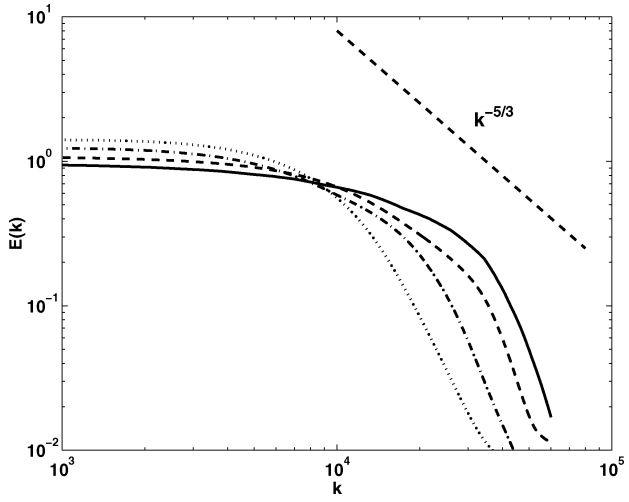

Fig. 19 Velocity spectra extracted from DSE05c at axial locations x/h: . . . . , 37.46; –·–, 40.09; – – –, 44.00; and ——, 46.60.

the subgrid model and the second-order scheme to form an inertial range. It is clearly observed, however, that the spectra shift to the higher wave numbers with increasing axial distance. This indicates that smaller scale vorticities are still generated when approaching the throat. Hence, the saturation of C_d only indicates that transition has slowed down, and we conclude that the turbulence state is still developing.

It is sufficient to mention that a parametric study has been conducted in the coarse grid configuration to investigate the effect of the injection fluctuation level, the energy subgrid models, and different subgrid stress models.[18] It was found that variation in the injection turbulence level has a strong effect only in the laminar and the beginning of transition region. In the turbulent region, no important difference was observed between 5 or 50% fluctuations level relative to the mean injection. The role of the energy subgrid models was not important, even in the highly compressible aft region. Dynamic Smagorinsky and dynamic mixed models for the subgrid stress tensor produced comparable results.

V. Summary

Compressible rocket flow simulations were conducted in laminar, transition, and turbulent regimes. The laminar simulation was performed using a direct simulation of the unsteady NS equations in two dimensions, whereas the transition and turbulent simulations were computed using a dynamic LES model. The results of the laminar case showed good agreement of the mean flow profiles with the inviscid theoretical profiles from Balakrishnan et al.,[2] which differ from Taylor's profile due to compressibility. The dimensional axial velocity and temperature also agree favorably. The effect of viscosity was found to be negligible because the corresponding inviscid simulation produced virtually the same results.

Comparing the unsteady component of the laminar flow with the acoustic-layer model of Majdalani and Van Moorhem[6] led to a good agreement in the irrotational as well as the rotational components within the first quarter of the chamber extent, which is equivalent to half of the acoustic wave length. Farther downstream, discrepancies appeared. A comparison with the stability analysis of Casalis et al.[19] showed possible interference of the natural instabilities of the flow with the acoustic waves. The interference is especially prominent for nondimensional angular frequency $\omega > 20$. This suggested that the comparison with the acoustic-layer model is restricted to low acoustic modes. Another possible source of disagreement is the nonuniformity of the medium in which the acoustic waves travel. The model is based on a constant speed of sound throughout the medium, whereas in the present compressible environment, it varys axially due to the decrease in the mean temperature. Further numerical investigations are required for guiding additional refinement of the acoustic model.

For the transition and turbulent cases, validation of LES in the CPR framework yielded satisfactory results. We assessed the grid dependency of LES in a rocket configuration mimicking the Traineau et al.[8] experiment. We found that increasing the axial resolution did not significantly change the mean flow prediction and the statistics in the turbulent region. However, it improved the statistical prediction in the laminar and transition regions substantially. We learned that the likelihood of the grid independency of LES to occur is the highest in the region where C_d is saturated after reaching the maximum value, that is, where the model contribution is maximum. In the region where C_d is still developing, the model contribution is smaller, and hence, the grid resolution should be adequate to capture the physics. A grid-refinement test is, therefore, more important in this transition region. As a consequence of the fact that LES is not designed to represent anisotropic disturbances in laminar and transition regions, these regimes could be more demanding in terms of grid resolution than the turbulent region. The limiting resolution of coarse grid LES in transitional flow is, hence, determined by the laminar and transition region. As an alternative to a grid-sensitivity test, a suitable resolution can be estimated by CPR validation in the transition region, that is, at ϵ value higher than used in the present validation.

The imposition of random fluctuations at the injection surface lacks a physical justification. A better way of modeling the injection process, which takes into account the spatial as well as time correlations of the fluctuations, is currently explored. This, together with forcing the inherent hydrodynamic disturbances could ease the resolution requirement of the laminar and transition region. The present study shows that LES with an efficient grid can produce comparable result to that of much finer grids reported in literature.

Acknowledgment

This research was funded by the U.S. Department of Energy through the University of California under Subcontract B341494.

References

[1]Beddini, R. A., "Injection-Induced Flows in Porous-Walled Ducts," *AIAA Journal*, Vol. 24, No. 11, 1986, pp. 1766–1773.

[2]Balakrishnan, G., Linan, A., and Williams, F. A., "Compressibility Effects in Thin Channels with Injection," *AIAA Journal*, Vol. 29, No. 12, 1991, pp. 2149–2154.

[3]Taylor, G. I., "Fluid Flow in Regions Bounded by Porous Surfaces," *Proceedings of the Royal Society of London, Series A: Mathematical and Physical Sciences*, Vol. 234, 1956, pp. 456–475.

[4]Flandro, G. A., "Effects of Vorticity on Rocket Combustion Stability," *Journal of Propulsion and Power*, Vol. 11, No. 4, 1995, pp. 607–625.

[5]Flandro, G. A., "On Flow Turning," AIAA Paper 95-2730, July 1995.

[6]Majdalani, J., and Van Moorhem, W. K., "Improved Time-Dependent Flowfield Solution for Solid Rocket Motors," *AIAA Journal*, Vol. 36, No. 2, 1998, pp. 241–248.

[7]Apte, S. V., and Yang, V., "Effects of Acoustic Oscillations on Turbulent Flowfield in a Porous Chamber with Surface Transpiration," AIAA Paper 98-3219, 1998.

[8]Traineau, J. C., Hervat, P., and Kuentzmann, P., "Cold Flow Simulation of a Two Dimensional Nozzleless Solid Rocket Motor," AIAA Paper 86-1447, June 1986.

[9]Apte, S. V., and Yang, V., "A Large-Eddy Simulation Study of Transition and Flow Instability in a Porous-Walled Chamber with Mass Injection," *Journal of Fluid Mechanics*, Vol. 477, 2003, pp. 215–225.

[10]Jameson, A., Schmidt, W., and Turkel, E., "Numerical Solutions of the Euler Equations by Finite Volume Methods Using Runge–Kutte Time-Stepping Schemes," AIAA Paper 81-1259, 1981.

[11]Ghosal, S., and Moin, P., "The Basic Equations for the Large Eddy Simulation of Turbulent Flows in Complex Geometry," *Journal of Computational Physics*, Vol. 18, 1995, pp. 24–37.

[12]Favre, A., "Turbulence: Space–Time Statistical Properties and Behaviour in Supersonic Flows," *Physics of Fluids A*, Vol. 3, 1983, pp. 2851–2863.

[13]Vreman, B., Geurts, B., Kuerten, H., Broeze, J., and Wasistho, B., "Dynamic Subgrid-Scale Models for LES of Transitional and Turbulent Compressible Flow in 3-D Shear Layers," *Proceedings of the 10th Symposium on Turbulent Shear Flows*, Pennsylvania State Univ., State College, PA, 1995, pp. 10.25–10.30.

[14]Germano, M., Piomelli, U., Moin, P., and Cabot, W. H., "A Dynamic Subgrid-Scale Eddy Viscosity Model," *Physics of Fluids A*, Vol. 3, 1991, pp. 1760–1765.

[15]Moin, P., Squires, K., Cabot, W., and Lee, S., "A Dynamic Subgrid-Scale Model for Compressible Turbulence and Scalar Transport," *Physics of Fluids A*, Vol. 3, 1991, pp. 2746–2757.

[16]Horiuti, K., "Large Eddy Simulation of Turbulent Channel Flow by One Equation Modeling," *Journal of the Physical Society of Japan*, Vol. 54, 1985, pp. 2855–2865.

[17]Venugopal, P., "Direct Numerical Simulation of Turbulence in a Model Solid Rocket Motor," Ph.D. Dissertation, Dept. of Theoretical and Applied Mechanics, Univ. of Illinois, Urbana, IL, Oct. 2003.

[18]Wasistho, B., Haselbacher, A., Najjar, F. M., Tafti, D., Balachandar, S., and Moser, R. D., "Direct and Large Eddy Simulations of Compressible Wall-Injection Flows in Laminar, Transitional, and Turbulent Regimes," AIAA Paper 2002-4344, July 2002.

[19]Casalis, G., Avalon, G., and Pineau, J. P., "Spatial Instability of Planar Channel Flow with Fluid Injection Through Porous Walls," *Physics of Fluids*, Vol. 10, No. 10, 1998, pp. 2558–2568.

T. Lin
Associate Editor